Total and regional microfiber transport characterization in a 15th - Generation human respiratory airway

Computers in Biology and Medicine 163 (2023) 107180

Contents lists available at ScienceDirect

Computers in Biology and Medicine

journal homepage: www.elsevier.com/locate/compbiomed

Total and regional microfiber transport characterization in a 15th - Generation human respiratory airway

Jiang Li [a], Jiawei Ma [b], Jingliang Dong [a], Wei Yang [c], Jiyuan Tu [a], Lin Tian [a,*]

[a] School of Engineering – Mechanical and Automotive, RMIT University, Bundoora, VIC, Australia
[b] Fusetec 3D Pty Ltd, Adelaide, SA, 5000, Australia
[c] Faculty of Architecture, Building and Planning, University of Melbourne, VIC, 3010, Australia

ARTICLE INFO

Keywords:
Fiber
Overall and regional deposition
Secondary flow
Fiber deposition pattern
Lobes deposition
Computational fluid dynamics

ABSTRACT

Fiber transport and deposition in the complete respiratory airway is of great significance for human health risk assessment. Thus far, the literature has mainly focused on limited branches of the upper airway and assumes spherical particles by neglecting fiber anisotropy. To fill the gap, this paper utilized an extended realistic respiratory airway from the nasal cavity to the distal bronchial tracts, up to the 15th generation. Fibers with aerodynamic diameters from 2 to 12 μm and aspect ratios of 1, 10, and 50 were released at the inlet of the respiratory airway model, and the coupled translational and rotational motion were computed. Overall and regional fiber deposition fractions, including the nasal cavities, laryngeal airway, and lungs were predicted and compared with earlier numerical results. The study also investigated: 1) secondary flow and distributions of the fibers at the lower respiratory airway entrance; 2) upstream conditions toward fiber deposition efficiencies; 3) fiber deposition patterns and detailed deposition fractions in the five lobes. Utilizing the realistic fiber transport model, the current study found that the upstream airway geometry and the flow condition have a significant impact on the fiber transport and deposition in the downstream airway regions. The fiber depositions in the lower and middle lobes are sensitive to the fiber aerodynamic diameter, but insensitive in the upper lobes. This study expects to generate innovative knowledge on the unique fiber motion characteristics toward potential inhalation health risks.

1. Introduction

Human respiratory airways have a high risk of infection as they are in direct contact with the atmosphere that may contain various hazardous aerosols. Human respiratory exposure to airborne elongated mineral particles (EMPs) is of particular interest due to severe adverse health consequences [1]. The occurrence of malignant respiratory diseases, such as lung cancer, mesothelioma, and asbestosis, has a close relationship with occupational exposure to asbestos, one of the most notorious EMPs [2,3]. Although the usage of asbestos has been strictly banned and the handling of existing materials is required to follow strict protocols, in most countries, new alternative materials, such as man-made vitreous fibers (MMVFs), carbon nanofibers, and carbon nanotubes are increasingly being utilized. The extremely small scale of these particles and their elongated needle-like appearance, like asbestos, have raised concerns of similar adverse health effects [4–6]. A report from the National Institute for Occupational Safety and Health (NIOSH) indicated that carbon nanotubes (CNTs) can result in lung inflammation, granuloma, and fibrosis based on animal studies. Other CNTs toxicity studies drew similar conclusions with lung inflammation, granuloma, and fibrosis observed in mice [7–10].

Particle deposition in human respiratory airways has been widely investigated in recent years. For spherical particles, Smith et al. compared the nanoparticle deposition in human lungs between a 3-year-old child and a 23-year-old young adult through an experimental measurement [11]. The results indicated that geometric variations between human subjects have a higher impact on particle deposition rate than the inhalation flow rate. Kelly examined micro-spherical particle deposition in two human nasal cavity replicas utilizing different stereolithography machines [12]. The results demonstrated that small differences in nasal cavity models can contribute to a significant difference in particle deposition. Garcia et al. investigated the nasal filtration of micron-ranged spherical particles by using five different nasal replicas, where the effects of the nasal filtration were measured by a series of

* Corresponding author.
E-mail address: lin.tian@rmit.edu.au (L. Tian).

https://doi.org/10.1016/j.compbiomed.2023.107180
Received 9 October 2022; Received in revised form 10 June 2023; Accepted 12 June 2023
Available online 13 June 2023

Stokes-based impaction parameters [13]. This study found that the usage of appropriate pressure-based impaction parameters can collapse the data in different nasal cavities to a single curve at varying flow rates. Rissler et al. recruited ten healthy volunteers to study human respiratory airway exposure to diesel exhaust particles [14]. Their results revealed that the common dose models, such as the multiple-path particle dosimetry, can accurately predict the deposition of diesel exhaust particles with the spherical particle assumption.

A few studies investigated the elongated particle, or fiber, deposition in respiratory tracts by in-vivo and in-vitro experiments. Timbrell, Lippmann, and Berman et al. reported that the deposition of fibers in the respiratory tracts could induce pathological changes [15–18]. Su and Cheng [19–21] investigated carbon micro-fiber deposition patterns in a human nasal replica at different flow rates. The results demonstrated that the inertia force dominates the fiber motion and deposition, and the anterior region of nasal cavities can easily trap micro-fibers with high inertia. Wang et al. utilized three realistic human nasal models made by stereolithography technology to investigate glass fiber deposition patterns at different flow rates [55]. This study also concluded that the micro-fiber deposition is sensitive to the impaction of particles, similar to the study of Su and Cheng [19–21].

In comparison to experiments, numerical measures, such as computational fluid dynamics (CFD), can predict more detailed quantitative data than traditional methods due to the limitations of high-precision measuring instrumentations. For example, numerical simulation can be applied to study the Ca^{2+} diffusion in human nervous systems [22,50]. A two-dimensional Ca^{2+} neuronal model was developed to investigate the Ca^{2+} spatiotemporal behaviors in neurodegenerative diseases [51]. A numerical simulation was performed to investigate the circulation flow and mass transfer inside atmospheric water drops (Wang et al.) [54]. In the field of inhalation studies, the prediction of spherical particle transport and deposition in human respiratory airways by CFD has been utilized in many years. Zhang et al. numerically built a four-generation airway model to study the nano-scale spherical particle deposition [23]. Their results indicated that the distribution of deposited nanoparticles is widely scattered in the human airway surface. Xu et al. investigated the inhalation health risk assessment for human tracheobronchial trees under particulate matter (PM) exposure at a bus stop scene [24]. Dong et al. simulated the spherical nanoparticle deposition in an extended large-to-small conducting lung airway model [25]. The results indicated that the inhalation flow rate plays a significant role in spherical particle deposition. Furthermore, Dong et al. evaluated the spherical particle deposition in two approximate upper tracheobronchial tree models and one realistic tracheobronchial airway model [26]. This investigation revealed that the airway model developed by Kitaoka (a semi-realistic airway using four algorithms [27]) can be used to predict reliable airflow and ultrafine particle motions.

The prediction of fiber deposition is more challenging compared to spherical particles since the coupled translation and rotation of the fiber are required in the simulation. Very few studies investigated the exact fiber motion in human respiratory tracts. Tian and Ahmadi [28,29] performed fiber transport and deposition simulations in a 2D duct and a 3D human lung bifurcation model. The hydrodynamic drag, shear-induced lift, and torque were considered. Single fiber trajectories were visualized. Effects of the airflow pattern, airway morphology, fiber size, and length on the ellipsoidal fiber deposition were investigated. Dastan et al. simulated the fiber deposition in three realistic human nasal airways at the airflow rates of 2.5, 5, 7.5, and 10 L/min per nostril [30]. Their results revealed that the Stokes-based aerodynamic diameter is an appropriate parameter to characterize the fiber deposition fraction. Tian and Ahmadi studied the effects of Brownian diffusion on nanofiber transport and deposition in human upper tracheobronchial airways [31,32]. It revealed that the Brownian excitation could either increase or suppress the fiber deposition according to a different combination of fiber diameters and lengths. Tavakol et al. studied impactions of turbulence fluctuations on fiber motion [33]. They found that turbulence fluctuations have strong effects on fibers with impaction parameters between 100 and 2000 $\mu m^2 \bullet L/min$. More recently, Li et al. evaluated the transport and deposition of fibers and spheres in a human nasal cavity model and a 2D channel [52,53]. Detailed effects of the fibrous particle size, length, rotation, and interaction with the local flow were analyzed. It was found that the fiber length is a key parameter affecting the micro-fiber motion and deposition in the human nasal cavity, and the shear-induced lift is important in certain scenarios. More details of the current state of the art on fiber transport and deposition can be found in the review work of Tian and Ahmadi [34].

It is seen that most of the prior studies were focused on the fiber motion in human nasal cavities, and very few studies investigated the fiber transport and deposition in the complete realistic respiratory airways from the nasal cavity to the distal bronchial tracts. Studies in the lower respiratory airways are extremely rare. Adverse respiratory health consequences may occur when a high penetration rate is observed for bio-persistent fibers while the human airway clearance mechanism is not able to remove them effectively. Detailed knowledge of the transport and deposition of elongated particles in human respiratory airways is of considerable importance to better assess the risks of human respiratory exposure to elongated particles. Along the inhalation pathway, mitigation and management of these risk scenarios can be effectively proposed.

In this study, the work of Li et al. was extended from nasal cavities to complete human respiratory airways up to the 15th generation [52]. The emphasis was on three local regions: the nasal cavities, the laryngeal, and the lower respiratory airways. The impact of the upstream airflow and fiber dynamics toward the lower airways was analyzed. The fibrous particle transport, rotation, and deposition were performed in a realistic human large-to-small conducting airway model. A constant inhalation breathing rate of 18 L/min was assumed, and the airflow field was evaluated under the $k-\omega$ SST model using the ANSYS FLUENT™ 19.2 (ANASYS., Lebanon, NH). A laminar-to-turbulent flow condition was simulated The coupled translation and rotation of the ellipsoidal fiber were modeled by using the ANSYS FLUENT™ User Defined Function (UDF), and the hydrodynamic drag, shear-induced lift, gravitational sedimentation, and torque experienced by each fiber were accounted for in the simulation. Deposition fractions of the fibrous particles in the human respiratory airways were predicted. Regional deposition efficiencies of fibers in the nasal cavities, laryngeal airway, and lungs were analyzed, and compared with earlier numerical results. Secondary flow and distributions of the fibers at cross sections of the lower respiratory airways, which have not been revealed in the past, were investigated and visualized. Deposition patterns and deposition characteristics of the micro-fibers in the five lung lobes were analyzed and discussed.

The potential impact of fibers on human health is crucial. The present work provides valuable insight to reveal the outcome of a complete human respiratory airway exposure to fibers, especially at distal bronchial tracts that is difficult to investigate by experiment. This study aims to generate innovative knowledge on the unique role of fibers toward deposition, and potentially improve the overall risk assessment capabilities.

2. Methodology

2.1. Computational model of the human respiratory airway

The realistic human respiratory tract used in this study is shown in Fig. 1. The geometry was originally reconstructed and validated by Shang et al. [36]. It has been used by Tu et al. [37], Dong et al. [25,38]. This airway model consists of the upper respiratory airway, including the nasal cavities, pharynx, larynx, and the lower respiratory airway extended from the trachea to terminal bronchioles up to the 15th generation. The geometric model is reconstructed from computed tomography (CT) scans of a healthy adult. Although a human bronchial tree consists of 23 generations from the trachea (generation 0) to the last terminal bronchioles (generation 23) [39], current geometry only

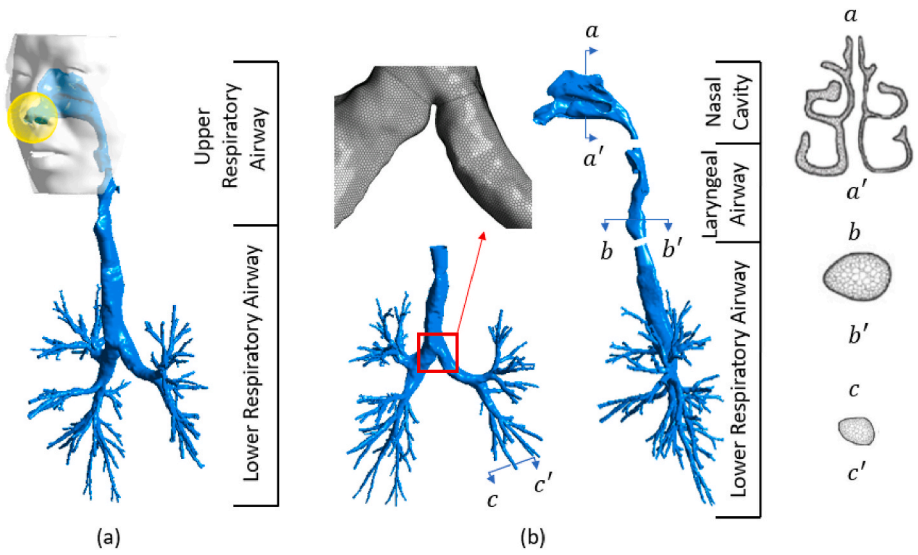

Fig. 1. Geometry of human respiratory airway and polyhedral mesh.

includes up to the 15th generation due to limitations of the CT image resolution. The airway model is meshed with polyhedral elements using ANSYS FLUENT™ 19.2 (ANASYS., Lebanon, NH). According to research from Ref. [40]; polyhedral elements are less sensitive to stretching and computationally less expensive when compared to other types of meshing elements. Prism layers (5 layers) are applied near the wall to accurately capture the boundary flow and particle behavior. Following a mesh independence test, approximately 2.9 million meshing cells are utilized in the current simulation. Cross-sectional meshing samples are shown in Fig. 1 (b) where 3 transverse slices at the locations $a-a'$, $b-b'$, and $c-c'$ are displayed. The detailed model reconstruction and verification can be found in the work of [25,36–38,41].

2.2. Fiber geometry and kinematic modeling

In this study, the micro-fiber is modeled as an elongated ellipsoid with a semi-major axis b and a semi-minor axis a, as shown in Fig. 2. Compared to spherical particles where only the translational motion is prescribed, the fiber motion requires the governing equations prescribing both the coupled translation and rotation due to the anisometric shape. Fiber kinematics is described by a set of coordinates (Fig. 2), where [x, y, z] is the global coordinate fixed in space, and $[\hat{x},\hat{y},\hat{z}]$ is attached to the fiber mass center with the coordinate axes parallel to the fiber's principal axes. Here the $\hat{z}$ axis superimposes the ellipsoid's major principal axis. A co-moving coordinate $[\hat{x},\hat{y},\hat{z}]$ is also attached to the fiber mass centroid, however with its coordinate axes parallel to the global coordinate [x, y, z]. The detailed kinematic relationship of the three coordinates can be found in the work of Li et al. [52], and also be found in the Appendix.

2.3. Governing equation of the fiber

2.3.1. Translational motion

The fiber, or ellipsoid particle, is acted upon by the air and gravity. Due to the shape of the ellipsoid particle, both the translational and rotational motion need to be resolved. A dilute condition is assumed where particle collisions are neglected. A creeping flow with a very low slipping velocity between the fiber and the air is assumed. The translation of an ellipsoid particle in a flow field is described as:

$$m^p\frac{d\boldsymbol{v}_f}{dt}=m^p\boldsymbol{g}+\boldsymbol{f}^h+\boldsymbol{f}^L \tag{1}$$

Where m^p is the particle mass expressed in Eq. (2), $\boldsymbol{v}_f$ is the particle centroid velocity, $\boldsymbol{g}$ is the gravitational acceleration, $\boldsymbol{f}^h$ and $\boldsymbol{f}^L$ are the hydrodynamic drag and shear-induced lift, respectively.

$$m^p=\frac{4}{3}\pi a^3\beta\rho^p \tag{2}$$

here β is the aspect ratio of the ellipsoid particle expressed as:

$$\beta=\frac{b}{a} \tag{3}$$

b and a are the semi-major and semi-minor axes, respectively.

[42] formulated the hydrodynamic drag $\boldsymbol{f}^h$ experienced by a small particle as:

$$\boldsymbol{f}^h=\mu\pi a\,\hat{\hat{K}}\cdot(\boldsymbol{u}_f-\boldsymbol{v}_f) \tag{4}$$

Where $\boldsymbol{u}_f$ and $\boldsymbol{v}_f$ ***are*** the flow and particle centroid velocity respectively. $\hat{\hat{K}}$ is the translational dyadic tensor given by Eq. (5):

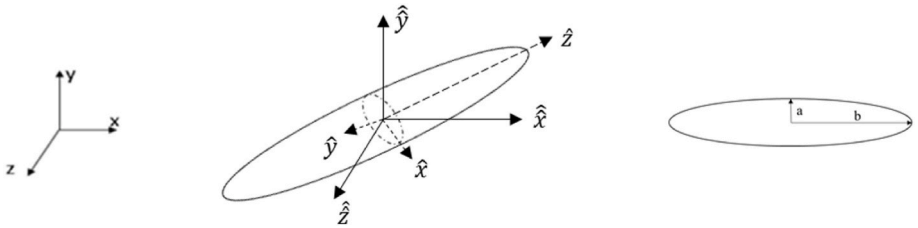

Fig. 2. Schematic of the coordinate systems of a fiber.

$$\widehat{\widehat{K}} = A^{-1}\widehat{K}A \tag{5}$$

Where $\widehat{K}$ is the diagonal matrix constituted by the diagonal elements $k_{\hat{x}\hat{x}}$, $k_{\hat{y}\hat{y}}$ *and* $k_{\hat{z}\hat{z}}$. For an ellipsoidal particle, the expression of $\widehat{K}$ is given by Refs. [43,44] as:

$$k_{\hat{x}\hat{x}} = k_{\hat{y}\hat{y}} = \frac{16\left(\beta^2-1\right)}{\left[\left(2\beta^2-3\right)ln\dfrac{\left(\beta+\sqrt{\beta^2-1}\right)}{\sqrt{\beta^2-1}}\right]+\beta} \tag{6}$$

$$k_{\hat{z}\hat{z}} = \frac{8\left(\beta^2-1\right)}{\left[\left(2\beta^2-1\right)ln\dfrac{\left(\beta+\sqrt{\beta^2-1}\right)}{\sqrt{\beta^2-1}}\right]-\beta} \tag{7}$$

[45] extended the shear-induced lift force $\boldsymbol{f^L}$ at low Reynold numbers as:

$$\boldsymbol{f^L} = \pi^2 a^2 \rho^p \sqrt{v} \bullet \boldsymbol{L_g} \tag{8}$$

Where $\boldsymbol{L_g}$ is the generalized lift vector given as:

$$\begin{aligned}\boldsymbol{L_g} = &\left[\frac{\dfrac{\partial u_x}{\partial y}}{\left|\dfrac{\partial u_x}{\partial y}\right|^2}\widehat{\widehat{k}} \bullet L_{xy} \bullet \widehat{\widehat{k}} + \frac{\dfrac{\partial u_x}{\partial z}}{\left|\dfrac{\partial u_x}{\partial z}\right|^2}\widehat{\widehat{k}} \bullet L_{xz} \bullet \widehat{\widehat{k}}\right] \bullet \begin{bmatrix} u_x - v_x \\ -v_y \\ -v_z \end{bmatrix} \\ &+ \left[\frac{\dfrac{\partial u_y}{\partial x}}{\left|\dfrac{\partial u_y}{\partial x}\right|^2}\widehat{\widehat{k}} \bullet L_{yx} \bullet \widehat{\widehat{k}} + \frac{\dfrac{\partial u_y}{\partial z}}{\left|\dfrac{\partial u_y}{\partial z}\right|^2}\widehat{\widehat{k}} \bullet L_{yz} \bullet \widehat{\widehat{k}}\right] \bullet \begin{bmatrix} -v_x \\ u_y - v_y \\ -v_z \end{bmatrix} \\ &+ \left[\frac{\dfrac{\partial u_z}{\partial x}}{\left|\dfrac{\partial u_z}{\partial x}\right|^2}\widehat{\widehat{k}} \bullet L_{zx} \bullet \widehat{\widehat{k}} + \frac{\dfrac{\partial u_z}{\partial y}}{\left|\dfrac{\partial u_z}{\partial y}\right|^2}\widehat{\widehat{k}} \bullet L_{zy} \bullet \widehat{\widehat{k}}\right] \bullet \begin{bmatrix} -v_x \\ -v_y \\ u_z - v_z \end{bmatrix}.\end{aligned} \tag{9}$$

Here $\boldsymbol{L_{xy}}, \boldsymbol{L_{xz}}, \boldsymbol{L_{yx}}\ \boldsymbol{L_{yz}}\ \boldsymbol{L_{zx}}\ \boldsymbol{L_{zy}}$ are the lift tensors of the ellipsoid particle, and calculated as:

$$\begin{aligned}\boldsymbol{L_{xy}} &= \begin{bmatrix} A & B & 0 \\ D & E & 0 \\ 0 & 0 & C \end{bmatrix} \\ \boldsymbol{L_{xz}} &= \begin{bmatrix} A & 0 & B \\ 0 & C & 0 \\ D & 0 & E \end{bmatrix} \\ \boldsymbol{L_{yx}} &= \begin{bmatrix} E & D & 0 \\ B & A & 0 \\ 0 & 0 & C \end{bmatrix} \\ \boldsymbol{L_{yz}} &= \begin{bmatrix} C & 0 & 0 \\ 0 & A & B \\ 0 & D & E \end{bmatrix} \\ \boldsymbol{L_{zx}} &= \begin{bmatrix} E & 0 & D \\ 0 & C & 0 \\ B & 0 & A \end{bmatrix} \\ \boldsymbol{L_{zy}} &= \begin{bmatrix} C & 0 & 0 \\ 0 & E & D \\ 0 & B & A \end{bmatrix}\end{aligned} \tag{10}$$

where $A = 0.0501$, $B = 0.0329$, $C = 0.0373$, $D = 0.0182$, *and* $E = 0.0173$.

2.3.2. Fiber rotational motion

The governing equations for the fiber rotational motion are:

$$I_{\hat{x}}\frac{d\omega_{\hat{x}}}{dt} - \omega_{\hat{y}}\omega_{\hat{z}}\left(I_{\hat{y}} - I_{\hat{z}}\right) = T^h_{\hat{x}} \tag{11}$$

$$I_{\hat{y}}\frac{d\omega_{\hat{y}}}{dt} - \omega_{\hat{z}}\omega_{\hat{x}}\left(I_{\hat{z}} - I_{\hat{x}}\right) = T^h_{\hat{y}} \tag{12}$$

$$I_{\hat{z}}\frac{d\omega_{\hat{z}}}{dt} - \omega_{\hat{x}}\omega_{\hat{y}}\left(I_{\hat{x}} - I_{\hat{y}}\right) = T^h_{\hat{z}} \tag{13}$$

Where $I_{\hat{x}}, I_{\hat{y}}$, *and* $I_{\hat{z}}$ are the fiber moments of inertia, $\omega_{\hat{x}}, \omega_{\hat{y}}$, *and* $\omega_{\hat{z}}$ are the angular velocities, and $T^h_{\hat{x}}$, $T^h_{\hat{y}}$, and $T^h_{\hat{z}}$ are the hydrodynamic torques acting on the fiber about its principal axis.

For the hydrodynamic torques, Jeffery proposed [43]:

$$T^h_x = \frac{16\pi\mu a^3\beta}{3\left(\beta_0+\beta^2\gamma_0\right)}\left[\left(1-\beta^2\right)d_{zy} + \left(1+\beta^2\right)\left(w_{zy}-\omega_x\right)\right] \tag{14}$$

$$T^h_y = \frac{16\pi\mu a^3\beta}{3\left(\alpha_0+\beta^2\gamma_0\right)}\left[\left(\beta^2-1\right)d_{xz} + \left(1+\beta^2\right)\left(w_{xz}-\omega_y\right)\right] \tag{15}$$

$$T^h_z = \frac{32\pi\mu a^3\beta}{3\left(\alpha_0+\beta_0\right)}\left(w_{yx}-\omega_z\right) \tag{16}$$

Where α_0, β_0, and γ_0 are the dimensionless parameters given by Eq. (17) and Eq. (18) [46], d_{zy}, d_{xz}, and w_{zy}, w_{xz}, w_{yx} are the deformation rate tensors and spin tensors of the fluid respectively (Eq. (19)).

$$\alpha_0 = \beta_0 = \frac{\beta^2}{\beta^2-1} + \frac{\beta}{2\left(\beta^2-1\right)^{\frac{3}{2}}}ln\left[\frac{\beta-\sqrt{\beta^2-1}}{\beta+\sqrt{\beta^2-1}}\right] \tag{17}$$

$$\gamma_0 = -\frac{2}{\beta^2-1} - \frac{\beta}{\left(\beta^2-1\right)^{\frac{3}{2}}}ln\left[\frac{\beta-\sqrt{\beta^2-1}}{\beta+\sqrt{\beta^2-1}}\right] \tag{18}$$

$$\begin{aligned} d_{\hat{z}\hat{y}} &= \frac{1}{2}\left(\frac{\partial u_{\hat{z}}}{\partial \hat{y}} + \frac{\partial u_{\hat{y}}}{\partial \hat{z}}\right) \\ d_{\hat{x}\hat{z}} &= \frac{1}{2}\left(\frac{\partial u_{\hat{x}}}{\partial \hat{z}} + \frac{\partial u_{\hat{z}}}{\partial \hat{x}}\right) \\ w_{\hat{z}\hat{y}} &= \frac{1}{2}\left(\frac{\partial u_{\hat{z}}}{\partial \hat{y}} - \frac{\partial u_{\hat{y}}}{\partial \hat{z}}\right) \\ w_{\hat{x}\hat{z}} &= \frac{1}{2}\left(\frac{\partial u_{\hat{x}}}{\partial \hat{z}} - \frac{\partial u_{\hat{z}}}{\partial \hat{x}}\right) \\ w_{\hat{y}\hat{x}} &= \frac{1}{2}\left(\frac{\partial u_{\hat{y}}}{\partial \hat{x}} - \frac{\partial u_{\hat{x}}}{\partial \hat{y}}\right) \end{aligned} \tag{19}$$

Here $\frac{\partial u_{\hat{z}}}{\partial \hat{y}}$, $\frac{\partial u_{\hat{y}}}{\partial \hat{z}}$, etc. are the velocity gradients given by

$$\widehat{G} = A\widehat{\widehat{G}}A^{-1} \tag{20}$$

Where $\widehat{G}$ and $\widehat{\widehat{G}}$ are the dyadic's expressed in the particle and co-moving coordinates, respectively.

2.4. Equivalent aerodynamic sphere

An equivalent diameter of a sphere is frequently proposed to characterize the motion of non-spherical particles. Researchers have introduced different equivalent diameters to study non-spherical particle deposition under different situations. For particles of large diameters, the main mechanisms contributing to the deposition are inertial impaction and gravity. Stober formulated an equivalent aerodynamic

diameter d_a to characterize the elongated ellipsoidal particles [47], which is widely used:

$$d_a = d_V\sqrt{\frac{\rho^p}{\rho_0 K_r}} \tag{21}$$

Where d_V is the diameter of a sphere with an equivalent volume, ρ^p is the particle density, ρ_0 is the density of water ($1000\ kg/m^3$), K_r is the dynamic shape factor of the ellipsoid, expressed as:

$$\frac{1}{K_r} = \frac{1}{3K_{\parallel}} + \frac{2}{3K_{\perp}}. \tag{22}$$

Here $K_\perp$ and $K_\parallel$ are the dynamic shape factors of the ellipsoid particle in the perpendicular and parallel orientations to the main flow direction. When the principal axis of the fiber is perpendicular to the mainstream, $K_\perp$ is given by:

$$K_{\perp} = \frac{8\left(\beta^2-1\right)\beta^{-\frac{1}{3}}}{3\left\{\left[\left(2\beta^2-3\right)ln\left(\beta+\sqrt{\beta^2-1}\right)\Big/\sqrt{\beta^2-1}\right]+\beta\right\}}.\# \tag{23}$$

When the principal axis of the fiber is parallel to the mainstream, $K_\parallel$ is given by

$$K_{\parallel} = \frac{4\left(\beta^2-1\right)\beta^{-\frac{1}{3}}}{3\left\{\left[\left(2\beta^2-1\right)ln\left(\beta+\sqrt{\beta^2-1}\right)\Big/\sqrt{\beta^2-1}\right]-\beta\right\}}. \tag{24}$$

2.5. The ellipsoid deposition scenarios

When a fiber comes into contact with a boundary, it is assumed to deposit due to the van der Waals adhesion force. Fiber orientation and its centroidal distance from the boundary determine the deposition criterion. Three fiber-boundary scenarios are listed: 1) if the centroidal distance from the boundary is smaller than fiber's semi-minor axis, deposition occurs; 2) if the centroidal distance from the boundary is larger than the semi-major axis, the particle is not deposited; 3) if the centroidal distance from the boundary is in between the semi-major and semi-minor axis, the fiber's orientation determines its deposition. Fig. 3 shows the deposition scenario 3. The inclination angle of the fiber to the boundary is $\frac{\pi}{2}-\alpha$, and the fiber capture distance d_V is defined as:

$$d_V = b\cos\alpha \tag{25}$$

Where cos α can be obtained as:

$$\cos\alpha = \frac{\overrightarrow{V_F}\bullet\overrightarrow{V_W}}{\left|\overrightarrow{V_F}\right|\times\left|\overrightarrow{V_W}\right|} \tag{26}$$

here $\overrightarrow{V_F}$ and $\overrightarrow{V_W}$ are the unit vectors of the fiber's principal axis and the wall-normal, respectively.

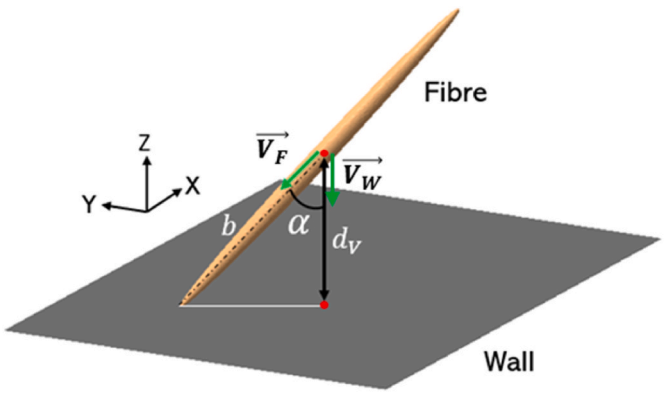

Fig. 3. Fibrous particle deposition schematics.

When the fiber centroidal distance from the boundary is smaller than the fiber's capture distance d_V, the fiber is considered deposited. The current study assumes that the deposited fibers will not re-enter the flow due to external forces.

3. Results and discussion

3.1. Airflow field simulation

In this study, a human nasal breathing rate of 18 L/min under normal breathing conditions is considered. To simulate the inhalation process, the inlet pressure is set as 0 Pa atmospheric at the nasal enclosure (Fig. 1a), while the outlet velocity is set at the bronchial exits to satisfy the breathing condition. The inhalation breathing air is assumed steady, laminar to turbulent in transition, incompressible, and isothermal. According to the equivalent lumen diameter and local velocity at cross-section b-b' (Fig. 1), the narrowest point in the larynx, the Reynolds number is calculated as 3000. The laminar-to-turbulent flow is simulated by using $k-\omega$ SST model [35], which has an accurate prediction of particle transport and has been widely used [35,48,49]. The density ρ of the airflow is $1.125 kg/m^3$, and the dynamic viscosity μ is $1.85\times10^{-5}\ Ns/m^2$.

Fig. 4 shows the flow field under a breathing rate of 18 L/min at the sagittal and coronal planes in the upper and lower respiratory airways respectively. Static air accelerates and enters the lateral vestibule, and expands into the main nasal passage at a low velocity (<2 m/s). The airflow accelerates along the posterior nasopharynx due to the bending and narrowing of the airway. Flow enters the laryngeal airway with a high velocity which forms the larynx jet, and a maximum velocity of 8 m/s is achieved at the larynx. Due to a gradual expansion following the laryngeal airway, the bulk flow slows down, and a fraction forms small vortices near the rugged wall. When the airflow enters the trachea, the bulk flow velocity drops to 2.5 m/s. The airflow continues developing in the trachea, where separations and recirculations are observed in the posterior trachea. The airflow slows down further through the right and left bronchus.

Fig. 5 shows the y^+ value of the airway model in the upper and lower respiratory airways respectively. Clearly seen, most of the airway region has very low y^+ (<1), and the highest y^+ is in the laryngeal region and is smaller than 4. This indicates a sufficient refinement of the flow field at the boundary to ensure an accurate near-wall resolution.

3.2. Total deposition efficiency

Carbon fibers of density 1830 kg/m^3 are grouped into three configurations based on the aspect ratio β (1,10,50). For each group, a series of aerodynamic diameters from 2 to 12 μm are included in the simulation. It should be noted that fibers with an aspect ratio of 1 are spherical particles.

Fig. 6 shows the predicted fiber deposition efficiencies versus the fiber aerodynamic diameters in the complete human respiratory airway at a breathing rate of 18 L/min. The deposition efficiency (DE) is defined in Eq. (27). For each configuration with a different aspect ratio, the DE curve grows steadily and monotonically with the aerodynamic diameters, indicating domination by the inertia. It is seen that the DE's are very low (<20%) when the fiber aerodynamic diameters are less than 3 μm for all three configurations. Beyond 3 μm, DE's of the fibers increase dramatically with the aerodynamic diameters up to 10 μm. At about 10 μm, the DE's of the fibers approach 90% and reach the maximum of 100% as the aerodynamic diameters arrive at 12 μm.

$$DE = \frac{the\ number\ of\ particles\ depositing\ in\ the\ local\ region}{the\ number\ of\ released\ particles\ in\ the\ inlet} \tag{27}$$

For fibers with aerodynamic diameters less than 4 μm, spherical

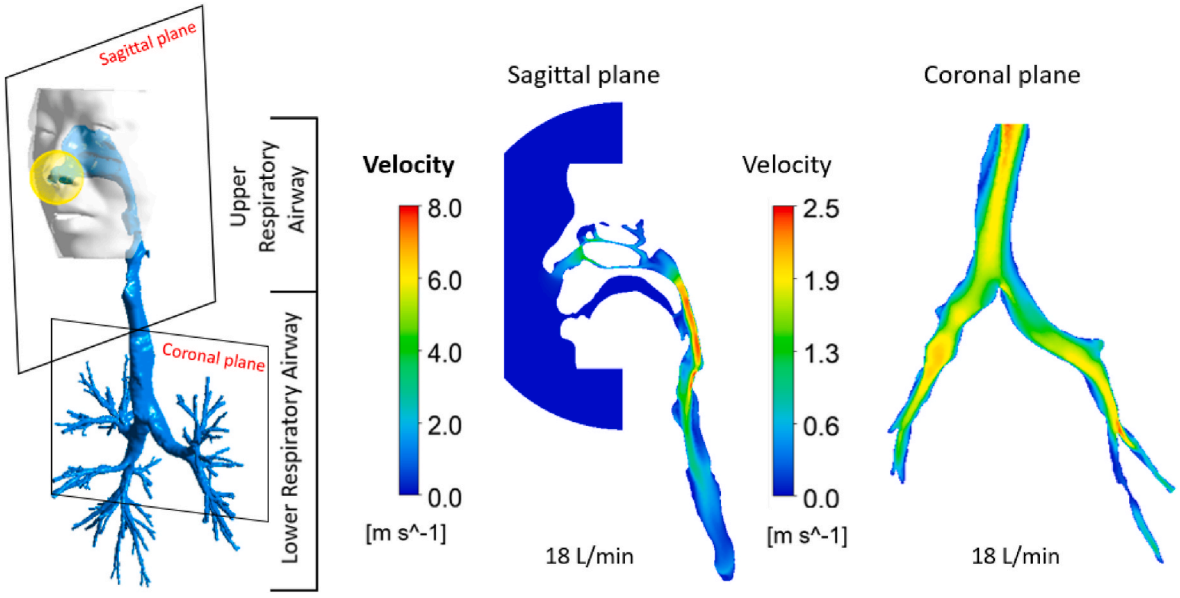

Fig. 4. Velocity magnitude contours of the extended respiratory airway model at selected cross-sections.

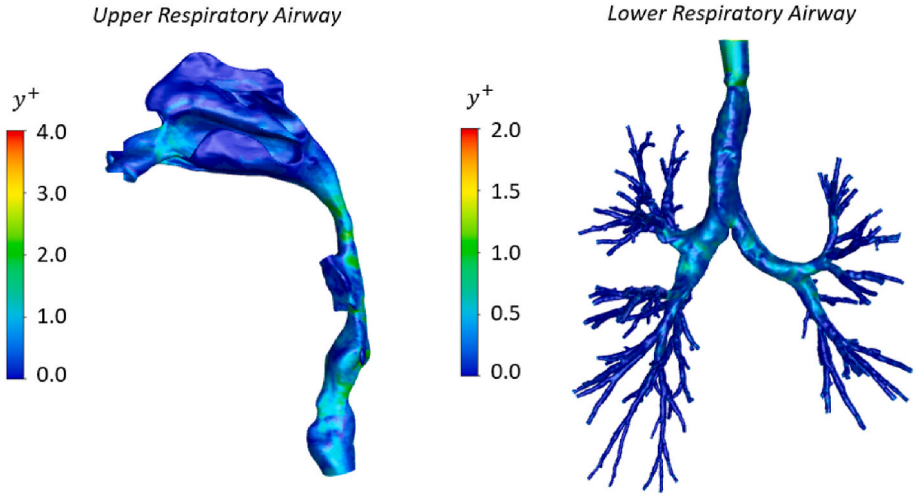

Fig. 5. *The* y^+ value of the airway model: a) upper respiratory airway; b) lower respiratory airway.

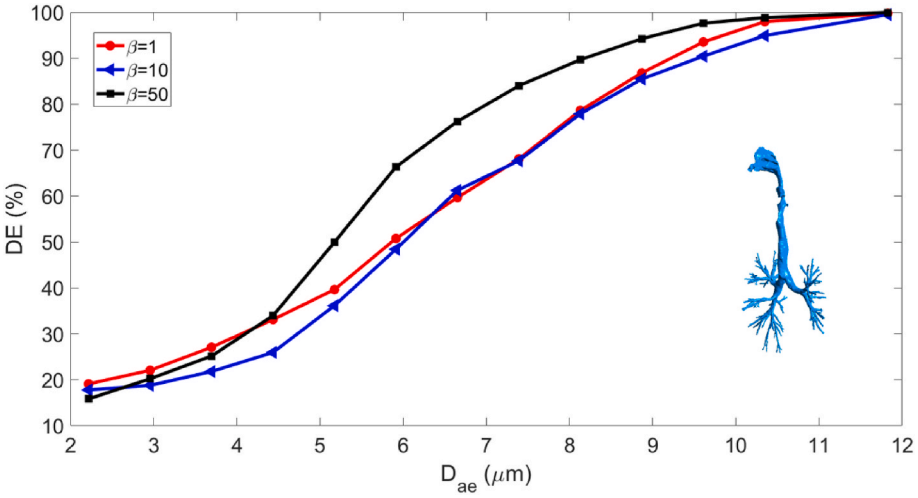

Fig. 6. Comparison of simulated fiber total deposition efficiencies versus aerodynamic diameter in the entire respiratory airway at a breathing rate of 18 L/min.

particles ($\beta = 1$) have the highest DE's. However, differences in the DE's among the three configurations are small and may indicate a limited impact on human health. For aerodynamic diameters from 4 to 10 μm, fibers with $\beta = 50$ have the highest DE's, and the DE's of fibers with $\beta = 1$ *and* 10 are about the same. The maximum difference between fibers with $\beta = 50$ *and* 1 reaches 40% at 6 μm. It can be concluded that the aerodynamic diameter alone is not sufficient to characterize fiber deposition in the human respiratory airways. The aspect ratio β, or the fiber length, has non-negligible effects in the particular aerodynamic diameter ranges. Longer fibers exhibit remarkably higher DE's than the shorter ones, especially for the aerodynamic diameters in the range from 5 to 9 μm. However, it is difficult to draw general conclusions since the deposition scenarios are drastically different in different respiratory regions. A detailed regional DE comparison should be performed for an accurate and reliable understanding.

3.3. Regional deposition efficiency

Simulated fiber DE's in the regional nasal cavity (blue shaded region, Fig. 7a) versus the fiber aerodynamic diameters at a breathing rate of 18 L/min are displayed in Fig. 7 (a). In general, DE's monotonically increase with the aerodynamic diameters for all three fiber configurations. The trends are similar to the overall DE's as shown in Fig. 6. Specifically, the DE's are about the same in the range from 2 to 4 μm. Beyond 4 μm, the DE's of the fibers with $\beta = 50$ increase dramatically until reaching 100% at 12 μm. The fibers with $\beta = 10$ have the lowest DE's below 6 μm, and they gradually surpass the DE's of the spherical particles ($\beta = 1$) with the increase of the aerodynamic diameters. At 12 μm, the DE's of the fibers with $\beta = 1$ *and* 10 both reach 90%. The nasal cavities have strong filtration capacity for the longer fibers with $\beta = 50$. Fewer fibers with long aspect ratios can enter the deep respiratory airways.

Fig. 7 (b) compares the predicted fiber DE's versus the impaction parameters (IP), defined as $d_{ae}^2 Q$, in the nasal cavity with data from previous simulations and experimental investigations [19,52]. Here d_{ae} is the aerodynamic diameter in μm, and Q is the breathing rate in ml/s. IP is frequently used for the dynamic characterization of inertial particles due to the combined effect of the diameters, sizes, material compositions, and flow conditions. A previous study by Li et al. used the same simulation method, however with a different nasal model [52]. In addition, the tracheobronchial airway is not included and the breathing rate is 15 L/min. The current prediction agrees very well with the prior studies. However, when the impaction parameter is larger than 2×10^4 $\mu m^2 ml/s$, the current prediction is higher which may be attributed to the difference in geometries and flow conditions.

The experimental results from Su and Cheng [19] are displayed in Fig. 7 (b) for comparison. In their study, carbon fibers (1830 kg/m^3), of a monodisperse diameter of 3.66 μm and polydisperse lengths and aspect ratios from 10 to 300 μm and 3 to 82, were released in a human nasal replica at breathing rates of 7.5, 15, 30 and 43.6 L/min respectively. The measured DE's of [19] exhibit a sharp increase at an impaction parameter of 1.5×10^4 $\mu m^2 ml/s$. When the impaction parameter is smaller than 1.5×10^4 $\mu m^2 ml/s$, the experimental results are similar to the current predictions of $\beta = 1$ *and* 10. When the impaction parameter is larger than 1.5×10^4 $\mu m^2 ml/s$, the results are similar to the current predictions of $\beta = 50$. We consider a reasonable agreement in trend versus the impaction parameters. The observed differences are mainly attributed to the intersubject variability in different nasal models.

Fig. 8 displays the predicted DE's of the fibers in the regional laryngeal airway (blue-shaded region, Fig. 8 (c)). For DE's versus the aerodynamic diameters in the laryngeal airway (Fig. 8 (a)), inverted U shapes are displayed. The DE's experience a steady increase in the aerodynamic diameters before the peak is reached around 7 μm. The longest fibers with $\beta = 50$ have the highest DE's when the aerodynamic diameter is below 5 μm, beyond that, DE's of $\beta = 50$ are exceeded by the fibers with $\beta = 1$ *and* 10, and they continue to increase until the peak value of 20% is reached around 6 μm. The DE's of $\beta = 50$ steadily decrease to 0% around 12 μm. On the other hand, the fibers with $\beta = 1$ *and* 10 have very similar DE's before reaching the peak values of 32% and 34% at 7 μm, respectively. After that, the DE's of the fibers with $\beta = 1$ *and* 10 decrease gradually to 5% at 12 μm. In the aerodynamic diameter range from 7 to 12 μm, DE's of the spherical particles ($\beta = 1$) is noticeably higher than the fibers with $\beta = 10$.

Below 5 μm, the fibers have very high penetration rates in the nasal airway as seen in Fig. 7 (a), since the fibers have a relatively low inertia when the aerodynamic diameter is below 5 μm. They tend to transport with the main flow instead of being captured by the wall due to gravity and inertia impaction. The unfiltered fibers enter the laryngeal airway, and their DE's increase with the aerodynamic diameters, indicating a more dominating inertia force. Beyond 5 μm, with the increase of DE's as shown in Fig. 7 (a), fewer fibers can penetrate into the laryngeal airway. This results in a decrease of DE's of the fibers in the regional laryngeal airway (Fig. 8 (a)). The observation implies that upper respiratory tracts have a significant impact on DE's of the fibers in lower respiratory airways.

To explicitly investigate fiber deposition in the laryngeal airway, a local deposition efficiency (LDE) is defined as:

$$LDE = \frac{\textit{the number of particles depositing in the local region}}{\textit{the number of particles entering the local region}}$$

Fig. 8 (b) displays the LDE's of the fibers versus the aerodynamic diameters in the local laryngeal airway. LDE's of all three fiber configurations increase gradually and steadily, and the differences are small when the fiber aerodynamic diameter is below 6 μm. Beyond 6 μm, fibers with $\beta = 1$ (or the spherical particles) take the lead and monotonically increase with the aerodynamic diameters until reaching 92% at 12 μm. Fibers with $\beta = 10$ *and* 50 experience a slower rate of increase of LDE's

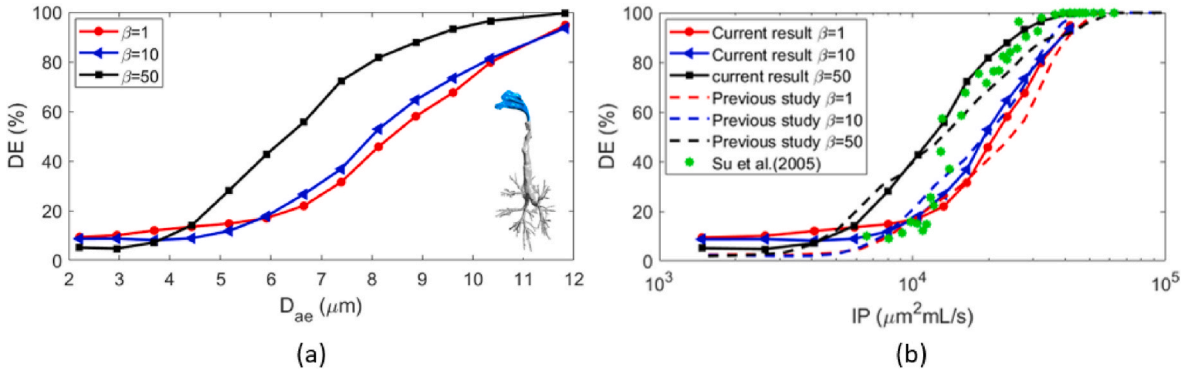

Fig. 7. Comparison of simulated fiber deposition efficiencies in the regional nasal cavities: a) fiber deposition efficiencies versus the aerodynamic diameter; b) fiber deposition efficiencies versus the impaction parameter (IP) – comparison with prior results.

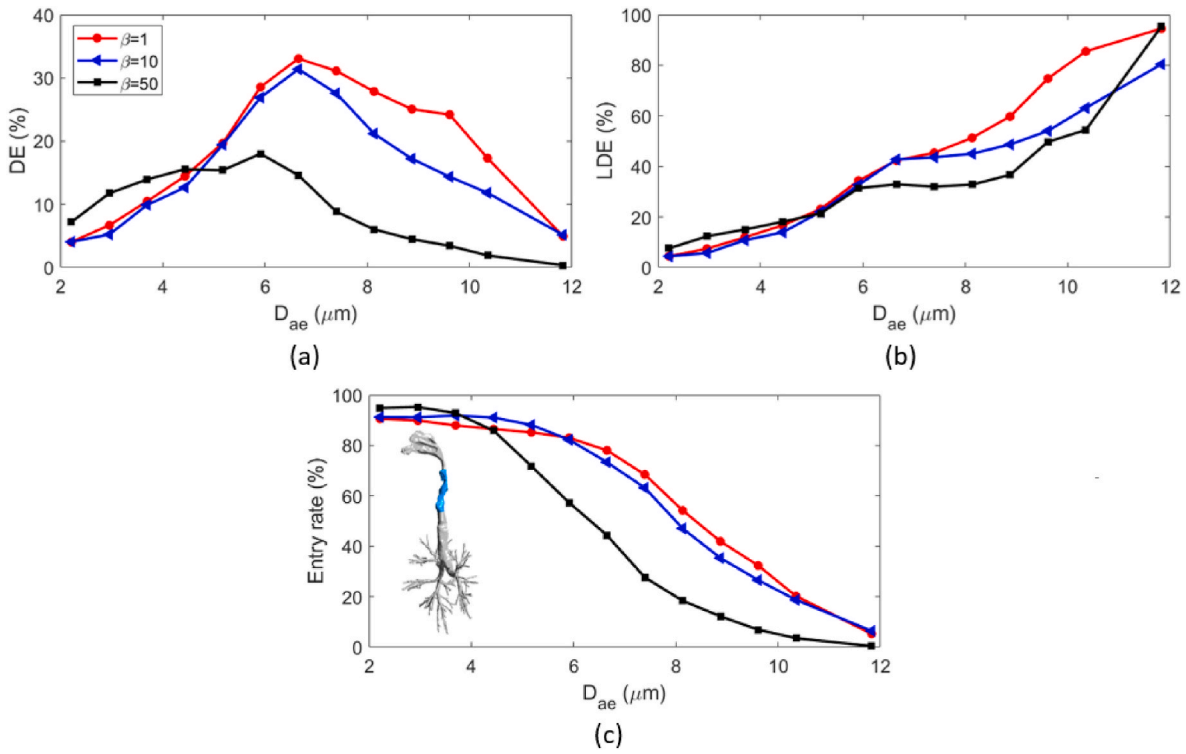

Fig. 8. Comparison of simulated fiber deposition efficiencies in the regional laryngeal airway: a) fiber deposition efficiencies; b) regional local deposition efficiencies (LDE); c) fiber entry rate to the regional airway.

from 6 to 10 μm. Beyond 10 μm, the LDE's of the fibers with $\beta = 50$ have a sharp increase and exceed that of the fibers with $\beta = 10$, and reach the same level as fibers with $\beta = 1$ (or the spherical particles). Overall, the three LDE curves show an inertial-dominated phenomenon, and the laryngeal airway has a high filtration capacity for large spherical particles.

To explicitly investigate the upstream-to-downstream influence on particle deposition, an entry rate is proposed as:

$$Entry\ rate = \frac{the\ number\ of\ particles\ entering\ the\ local\ region}{the\ number\ of\ total\ released\ particles\ at\ the\ inlet}$$

The entry rate is a good indication of the accessibility of the initially released particles to the downstream regions. A low entry rate implies a high upstream filtration capacity due to the combined effect of geometry and flow complexity. A low entry rate results in a more complex particle flow condition in the downstream locations.

Fig. 8 (c) shows the fiber entry rates versus the aerodynamic diameters in the laryngeal airway. Clearly seen, all curves decrease with the aerodynamic diameters. Below 4 μm, the fibers have very high entry rates about 90%. It is apparent that the human nasal cavities cannot effectively filter out fibers with aerodynamic diameters smaller than 4 μm. However, with the increase of the aerodynamic diameter, fiber entry rates decrease rapidly, especially for the longest fibers with an aspect ratio of 50. This implies that the very long fibers have a lower chance to penetrate deeper respiratory airways. Fibers with $\beta = 50$ can hardly propagate into the laryngeal airway when the aerodynamic diameter is above 10 μm.

Fig. 9 shows fiber transport and deposition in the lower respiratory airway. The entry rates of all fibers entering the lower respiratory airway are the highest at 88% at 2 μm and decrease gradually with the increase of the aerodynamic diameters (Fig. 9 (a)). The entry rate profiles of the three fiber configurations are similar and high around 80–90% when the aerodynamic diameters are below 4 μm (Figs. 9 (a) and Fig. 8 (c)). The entry rates of all fibers with a small aerodynamic diameter of less than 4 μm are insensitive to the aspect ratio, aerodynamic diameter, and airway geometry. Small fibers have strong flowability, and they can propagate with the main flow without being deposited. Beyond 10 μm, the fibers have very low entry rates (<10%).

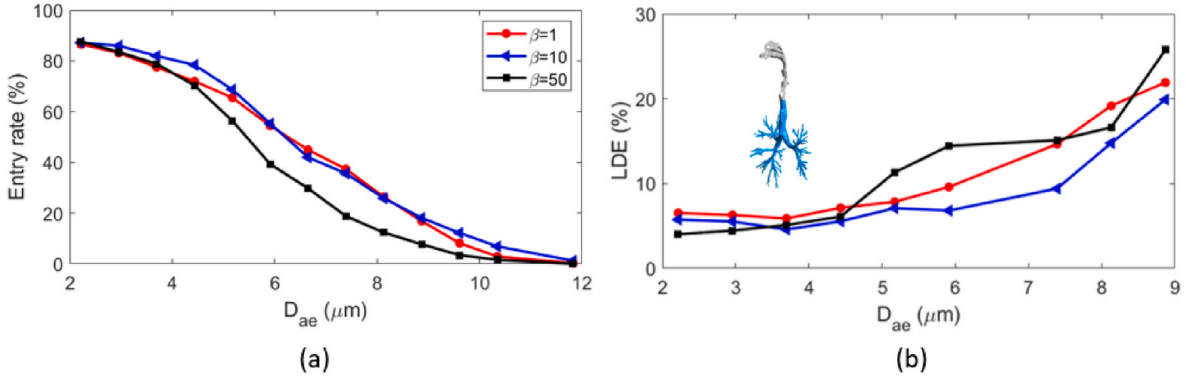

Fig. 9. Comparison of simulated fiber deposition efficiencies in the lower respiratory airway: a) fiber entry rate; b) fiber local deposition efficiencies.

At aerodynamic diameters around 10 μm, most of the fibers are filtered by the nasal cavities and the laryngeal airway. It is seen from Fig. 9 (a), fibers with $\beta = 1$ *and* 10 have the highest entry rates. It is concluded that the shorter fibers have higher penetration rates in the human respiratory tracts, and are easier to penetrate the deeper airways. On the other hand, the longest fibers with $\beta = 50$ have the lowest entry rates among all examined aerodynamic diameters. In upper nasal airways, the airflow is complex with sharp changes of angles. This results in high shear and high vortices. The current study shows that the fibers with larger aspect ratios have a higher possibility to get deposited in the upper airways. The extremely long fibers are difficult to propagate into the lungs. When the aerodynamic diameter is above 9 μm, entry rates of the fibers with $\beta = 50$ are less than 5%. They may pose less risk to human lower respiratory systems when compared to spheres and shorter fibers.

Fig. 9 (b) displays the LDE's of the fibers versus the aerodynamic diameters in the lower respiratory airway. The LDE's of all fibers are consistently very low (about 5%) when the aerodynamic diameters are below 5 μm. Beyond 5 μm, the LDE's of the fibers steadily increase with the aerodynamic diameters. Particularly for the fibers with $\beta = 50$, the LDE's increase rapidly to 15% at 6 μm. After that, a steady increase is seen from 6 μm to 8 μm before the LDE's reach the highest value of 25% at 9 μm. Fibers with $\beta = 10$ have the lowest LDE's among all fiber configurations and reach a peak value of 20% at 9 μm. Due to the low LDE's and the high entry rates of fibers with $\beta = 10$, a higher proportion of the fibers with $\beta = 10$ can spread into the alveoli region. Spherical particles ($\beta = 1$) have the highest LDE's among all configurations when the aerodynamic diameters are below 4.5 μm. and beyond that, two crossovers with fibers of $\beta = 50$ are observed. Fiber deposition efficiencies are complicated to predict in the lungs as a result of the impaction from the upstream. A similar observation can be made in Fig. 8 (b), where the LDE curves of the fibers with $\beta = 10$ *and* 50 have a slower rate of when the aerodynamic diameters are between 6 and 8 μm. This indicates that fibers are more sensitive to the upstream impaction than spherical particles, as the orientation is an additional contributing factor to the deposition. Although the LDE's of the spherical particles are slightly lower than the fibers with $\beta = 50$, it is difficult to conclude that the fibers with $\beta = 50$ have a lower potential risk in the human lower respiratory airways, as the spherical particles have higher entry rates. The spherical particles ($\beta = 1$) and fiber of $\beta = 50$ may have a similar impact on human health. Further investigations are needed.

To evaluate the effect of fiber initial release position on fiber LDE's, Fig. 10 plots fiber LDE's versus the aerodynamic diameters in the lower respiratory airway with two different release profiles. The solid lines represent fiber LDE's resulting from an initial release from the usual breathing zone outside the nostrils (Fig. 10, yellow release profile, top illustration), while the dashed lines indicate the LDE's of the fibers released uniformly from the entrance of the lung with the local flow velocity as shown in Fig. 10 (yellow release profile, bottom illustration). In Fig. 10, all LDE curves start at about 5% at 2 μm and grow slowly. Clearly seen from Fig. 10 that, without the upstream influence (fibers released uniformly from the lung entrance), LDE's of the fibers are markedly smoother than the fibers released from the breathing zone. Similarly, the steady and monotonically increased LDE's against the aerodynamic diameters indicate an inertia-dominated deposition process. In summary, fibers with $\beta = 50$ have the lowest LDE's when $D_{ae} <$ 4 μm, however, the LDE's grow and exceed the fibers with $\beta = 10$ when $D_{ae} >$ 5 μm. Spherical particles have the highest LDE's when the aerodynamic diameters are below 5 μm, beyond that, LDE's of the spherical particles ($\beta = 1$) are similar to that of the fibers with $\beta = 10$. Differences between the solid and dashed lines are obvious when the aerodynamic diameter is greater than 5 μm. For the same aspect ratio of $\beta = 50$, the fibers released from the nasal breathing zone have higher LDE's than the release profile from the lung entrance. A similar observation is made for the spherical particles ($\beta = 1$). However, for fibers with $\beta = 10$, an opposite trend is seen. Fibers released at the lung entrance have higher LDE's than fibers released from the breathing zone. This difference implies that the upstream conditions have a great impact on the downstream fiber deposition. Therefore, it is important to taking account the upper respiratory airway effects when studying the deposition characteristics of fibers in the lower respiratory airways.

Fig. 11 shows the fiber transport profiles and secondary airflow streamlines at the cross-section of the tracheobronchial entrance. The initial fiber-releasing position is from the breathing zone outside the nostrils (Fig. 1 (a)). The profiles (Fig. 11 (a)) show that most of the fibers concentrated along the bottom edge of the cross-section (front chest), especially for high-inertia fibers with $\beta = 50$ or $D_{ae} = 8$ μm (Fig. 11 (a3), (a6), (a7), (a8), (a9)), where the LDE's are also high as shown in Fig. 10. Compared with the case of uniform releasing from the lung entrance (not displayed), fiber distribution is significantly different, leading to the different LDE's in Fig. 10. Meanwhile, a large number of fibers with $\beta =$ 1 and 10 transports through the lower left corner of the cross-section (front right chest side), especially for smaller $D_{ae}{}'s$ of 6 μm and 8 μm (Fig. 11 (a1), (a2), (a4), (a5)). Fiber distributions at the cross section are highly correlated to the high-inertia regions as indicated by the cross-plane airflow streamlines as shown in Fig. 11 (b). The secondary flow has a great influence on fiber transport profiles in the tracheobronchial airways. Two apparent vortexes are observed at the top corner of the cross-section (back chest), where the fibers tend to follow the vortexes, especially for fibers with smaller aerodynamic diameters ($D_{ae} = 6$ μm and 8 μm). As seen, the inertia-dominated fibers tend to accumulate to

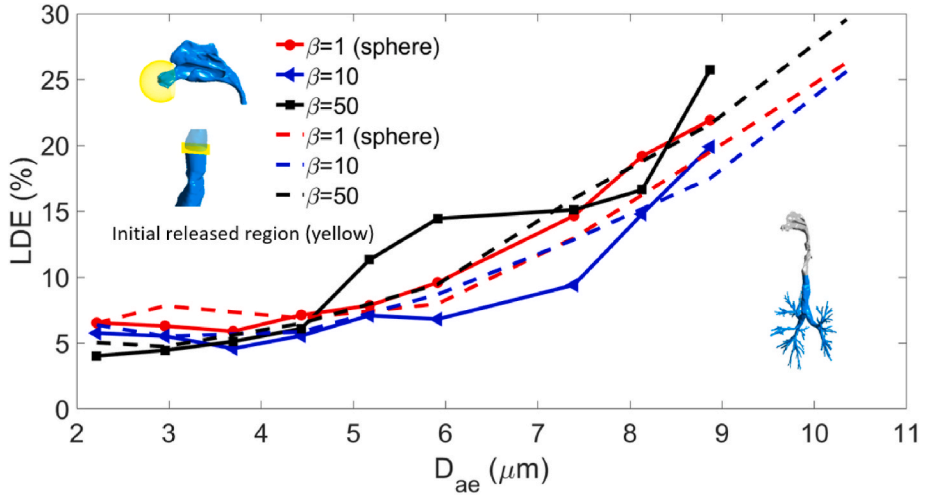

Fig. 10. Comparison of fiber local deposition efficiencies (LDE's) in the lungs with different initial release profiles.

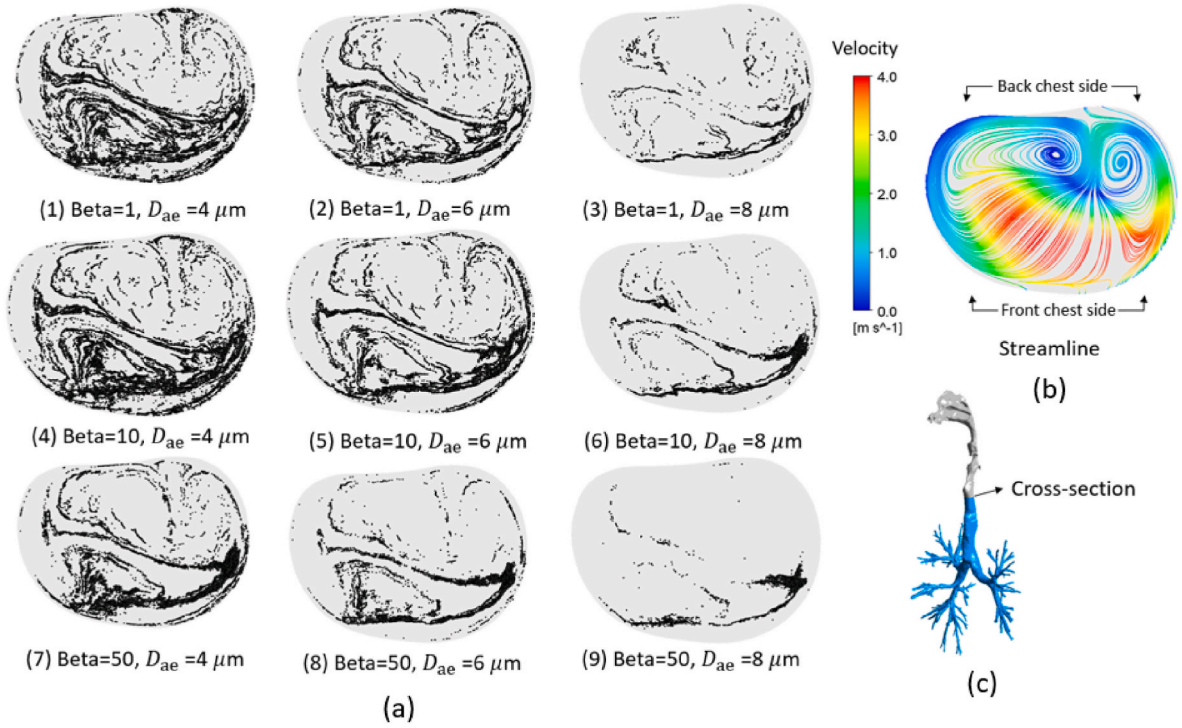

Fig. 11. Fiber transport profiles and the secondary airflow streamlines at the cross-section of the tracheobronchial entrance: a) fiber transport profile; b) secondary airflow streamlines; c) cross-section location.

the front chest after impinging the right wall, which leads to an apparent third vortex when the fibers leave the region. The non-uniform fiber distributions and the secondary flow drive the fibers into complex trajectories and induce additional depositions in the lungs. It is important to account for the upstream effect to study fiber transport and deposition in downstream airways.

3.4. Fiber deposition patterns

Fig. 12 compares the global deposition patterns of the fibers with $\beta =$ 10 and $D_{ae} = 4$ μm, 6 μm, and 8 μm, respectively. Deposition patterns of other fiber configurations are performed however not shown due to the space limitation. Medium-length fibers with $\beta = 10$ are chosen to present the fiber deposition characteristics, and the fibers with small-to-large aerodynamic diameters of 4 μm, 6 μm, and 8 μm are representative corresponding to the variations of DE's and LDE's in Figure 6–10. It can be seen that fiber depositions mainly concentrate in the vicinity of the nasal vestibule, middle and inferior nasal meatus, glottis and subglottis, proximal trachea, and five lung lobes. With an increase of the aerodynamic diameter, the deposited fibers tend to be more concentrated, and the deposition "hot spots" resemble each other regardless of the fiber sizes. The compartment deposition fractions of the nasal cavities, laryngeal airway, and lower respiratory airway are summarised and displayed in Fig. 12. For fibers with $D_{ae} = 4$ μm and 6 μm, the laryngeal airway has the highest deposition fractions (48.8% and 55.5%), due to a bending geometry of the glottis. For fibers with $D_{ae} = 8$ μm, under the action of a high inertial force, the nasal cavities capture most of the fibers (75.7%). The deposition fraction is the lowest in the

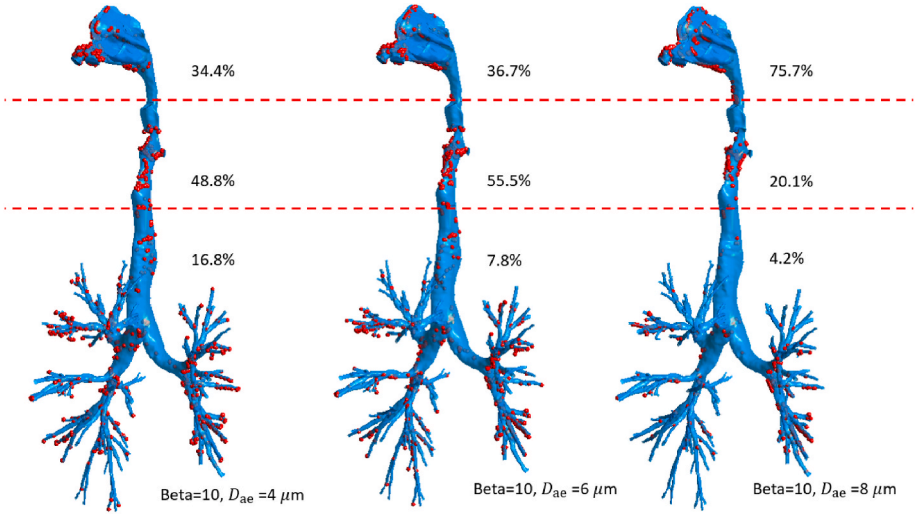

Fig. 12. Global deposition patterns of the fibers.

Table 1
Local deposition efficiencies (LDE's) of the fibers in five lobes.

Location	D_{ae} = 4 μm	D_{ae} = 8 μm
LUL	6.8%	4.7%
LLL	18.8%	47.3%
TOT	25.6%	52.0%
Location	D_{ae} = 4 μm	D_{ae} = 8 μm
RUL	14.1%	15.1%
RML	4.9%	17.3%
RLL	29.1%	3.6%
TOT	48.1%	36.0%

lower respiratory airway regardless of the fiber size and the fiber deposition fractions are gradually decreasing with the increase of the diameter due to the upstream impact.

Detailed deposition data (LDE's) of the fibers with $\beta = 10$ in the five lung lobes up to the 15 generations are presented in Table 1. It is seen that, with the aerodynamic diameter increasing from 4 to 8 μm, the LDE's in the left upper lobe (LUL) have a minor decrease from 6.8% to 4.7%, while in the left lower lobe (LLL) incease dramatically from 25.6% to 52.0%. The LDE's in the right upper lobe (RUL) remain unchanged when the aerodynamic diameter increases. The LDE's in the right middle lobe (RML) increase from 4.9% to 17.3% with the aerodynamic diameter, while in the right lower lobe (RLL) an opposite trend from 29.1% to 3.6% is displayed. Clearly seen that the LDE's in the lower and middle lobes are sensitive to the aerodynamic diameter size, while not sensitive in the upper lobes. On the other hand, the total LDE's in the left lobes increase with the aerodynamic diameter, while they decrease in the right lobes. According to fiber cross-sectional distributions as shown in Fig. 11 (a4) and (a6), the fibers in the vicinity of the right chest are decreasing when the aerodynamic diameter increases; however, the fibers in the vicinity of the left chest remain unchanged. The secondary flow in the airway affects the fiber entry profile in the lower respiratory airways, and results in the variation of LDE's in the left and right lobes. Again, the complex upstream geometry and flow condition will have an impact on the downstream fiber transport outcomes.

4. Conclusion

In this study, the transport and deposition of ellipsoidal particles were systematically investigated in an extended human respiratory airway model. The physiologically realistic anatomical airway model up to the 15th generation, developed by Ref. [36]; was used in the present study. This model reconstruction via the CT image scans captured the fine anatomical features of the human respiratory airways and optimized the airway structure for digital analysis. The airway model was divided into three compartments, including the nasal cavities, laryngeal airway, and tracheobronchial tree up to the 15th generation. The fiber deposition efficiencies in the whole tracts and the specific regions were numerically examined. Fiber transportation profiles at the selected airway cross sections were studied.

The proposed human respiratory airway modeling approach is a cost-effective way to perform the risk assessment and evaluate human respiratory exposure to fibers. The innovative knowledge of the unique characteristics of fibers toward potential health risks can be extracted from the fiber transport, rotation, and deposition in the complete and regional human respiratory airways. The study found that, in human nasal cavities, the longest fibers with $\beta = 50$ have the highest deposition efficiencies in a large range of aerodynamic diameters. In the laryngeal airway, the spherical particles have the greatest deposition efficiencies, while in the lower respiratory airway, it is difficult to conclude. The combined effects of the geometry and secondary flow complexity result in a multifaceted fiber deposition trend in the lower respiratory airways. Three distinct regions can be identified based on deposition classifications in the laryngeal and lower respiratory airways: a) for aerodynamic diameters <6 μm, the deposition efficiencies increase with the aerodynamic diameters gradually; b) in the mid-range between 6 μm and 8 μm, the deposition efficiencies are steady; c) for aerodynamic diameters >8 μm, the deposition efficiencies increase rapidly until reaching 100%. Fiber deposition characteristics are significantly impacted by the upstream conditions, such as the geometry, secondary flow, upstream distribution, and orientation of the fibers. It is important to account for the upstream impact, especially for high-inertia fibers with large aspect ratios and aerodynamic diameters. In addition, the nasal cavities and larynx airway have a strong filtration capacity that blocks the high-inertia fibers from propagating into the deep lungs. The fibers with smaller aspect ratios and aerodynamic diameters have higher entry rates into the human deeper respiratory tracts. Fibers with large aspect ratios and aerodynamic diameters may have a higher possibility to cause infections in the nasal cavities and larynx airway, while fibers with smaller aspect ratios and aerodynamic diameters could be more dangerous to the deep lungs and alveolars.

Based on the outcomes of the regional deposition characteristics, it was found that fibers with different lengths however of the same aerodynamic diameter could have different deposition efficiencies. The aerodynamic diameter alone is not sufficient to characterize fiber deposition in the human respiratory tracts. Additional investigations are needed to clarify this point further. Last but not least, according to the investigation of local deposition efficiencies in the five lobes, LDE's of the lower and middle lobes are sensitive to the aerodynamic diameter, while they are less affected in the upper lobes. The LDE's in the right and left lobes are clearly impacted by the fiber size and upstream cross-sectional flow and fiber conditions at the trachea entrance.

Declaration of competing interest

The authors declare that they have no known competing financial interests or personal relationships that could have appeared to influence the work reported in this paper.

Acknowledgements

The financial support provided by the Australian Research Council (Grant No. DE180101138, DE210101549) are gratefully acknowledged.

Appendix

Fiber kinematic transformation

The kinematic transformation between the fiber's co-moving coordinate $[\hat{x}, \hat{y}, \hat{z}]$ and the fiber coordinate $[\hat{x}, \hat{y}, \hat{z}]$ is shown as:

$$\hat{\mathrm{x}} = \mathrm{A}\hat{\hat{\mathrm{x}}} \tag{A1}$$

where $\mathrm{A} = [a_{ij}]$ is the transformation matrix between $[\hat{x}, \hat{y}, \hat{z}]$ and $[\hat{\hat{x}}, \hat{\hat{y}}, \hat{\hat{z}}]$, and it can be described in terms of the Euler angles [56–58]:

$$\boldsymbol{A} = \begin{bmatrix} \cos\psi\cos\varnothing - \cos\theta\sin\varnothing\sin\psi & \cos\psi\sin\varnothing + \cos\theta\cos\varnothing\sin\psi & \sin\psi\sin\theta \\ -\sin\psi\cos\varnothing - \cos\theta\sin\varnothing\cos\psi & -\sin\psi\sin\varnothing + \cos\theta\cos\varnothing\cos\psi & \cos\psi\sin\theta \\ \sin\theta\sin\varnothing & -\sin\theta\cos\varnothing & \cos\theta \end{bmatrix} \tag{A2}$$

where, ψ, $\varnothing$ and θ are Euler angles shown in Figure A1 (a).

Due to the occurrence of singularity, alternatively, Euler's four parameters (quaternions) are used in defining the transformation matrix [56–58], and given as:

$$A = [a_{ij}] = \begin{bmatrix} 1-2(\varepsilon_2^2+\varepsilon_3^2) & 2(\varepsilon_1\varepsilon_2+\varepsilon_3\eta) & 2(\varepsilon_1\varepsilon_3-\varepsilon_2\eta) \\ 2(\varepsilon_2\varepsilon_1-\varepsilon_3\eta) & 1-2(\varepsilon_3^2+\varepsilon_1^2) & 2(\varepsilon_2\varepsilon_3+\varepsilon_1\eta) \\ 2(\varepsilon_3\varepsilon_1+\varepsilon_2\eta) & 2(\varepsilon_3\varepsilon_2-\varepsilon_1\eta) & 1-2(\varepsilon_1^2+\varepsilon_2^2) \end{bmatrix} \tag{A3}$$

where $\varepsilon_1, \varepsilon_2, \varepsilon_3, \eta$ are the Euler's four parameters and the relation to the ellipsoid rotation vector **e** and rotation angle $\boldsymbol{\Omega}$ is illustrated in Figure A1 (b).

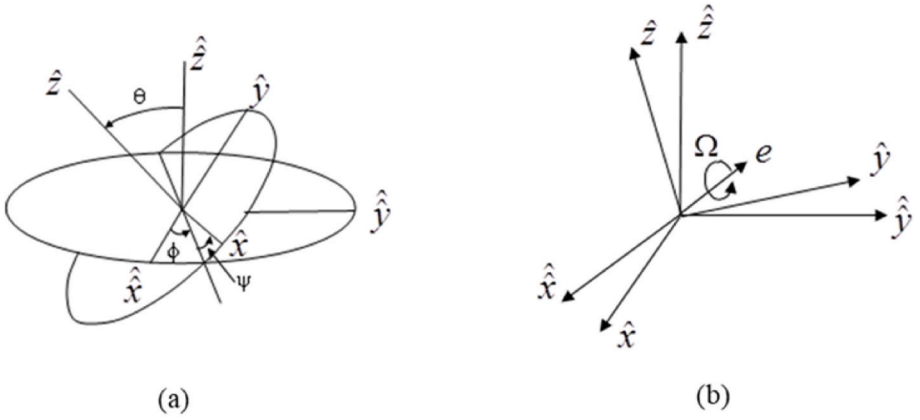

Fig. A1. Transformation of coordinate systems: (a) Euler angles and (b) Euler's four parameters

The relationship between the Euler's four parameters, rotation vector and angle are described in Eqs. (A4) to (A5). The Euler's four parameters also follow the constrain of the rotation of a rigid body in the three-dimensional coordinate, expressed in Eq. (A6).

$$\begin{bmatrix} \varepsilon_1 \\ \varepsilon_2 \\ \varepsilon_3 \end{bmatrix} = \boldsymbol{e}\ sin\left(\frac{\Omega}{2}\right) \tag{A4}$$

$$\eta = cos\left(\frac{\Omega}{2}\right) \tag{A5}$$

$$\varepsilon_1^2 + \varepsilon_2^2 + \varepsilon_3^2 + \eta^2 = 1 \tag{A6}$$

The Euler's four parameters are related to the elements of the transformation matrix $A = [a_{ij}]$. If $\eta \neq 0$,

$$\eta = \pm\frac{1}{2}(1 + a_{11} + a_{11} + a_{11})^{\frac{1}{2}} \tag{A7}$$

$$\begin{bmatrix} \varepsilon_1 \\ \varepsilon_2 \\ \varepsilon_3 \end{bmatrix} = \frac{1}{4\eta}\begin{bmatrix} a_{23} - a_{32} \\ a_{31} - a_{13} \\ a_{12} - a_{21} \end{bmatrix}. \tag{A8}$$

If $\eta = 0$,

$$\varepsilon_1 = \pm\sqrt{\frac{1 + a_{11}}{2}} \tag{A9}$$

$$\varepsilon_2 = \frac{a_{12}}{2\varepsilon_1} \tag{A10}$$

$$\varepsilon_3 = \frac{a_{23}}{2\varepsilon_2}. \tag{A11}$$

The angular velocity ω_i can be described as the time rate of change of the Euler's four parameters, given by Eq. (A12).

$$\begin{bmatrix} \frac{d\varepsilon_1}{dt} \\ \frac{d\varepsilon_2}{dt} \\ \frac{d\varepsilon_3}{dt} \\ \frac{d\eta}{dt} \end{bmatrix} = \frac{1}{2} \begin{bmatrix} \eta\omega_{\hat{x}} - \varepsilon_3\omega_{\hat{y}} + \varepsilon_2\omega_{\hat{z}} \\ \varepsilon_3\omega_{\hat{x}} + \eta\omega_{\hat{y}} - \varepsilon_1\omega_{\hat{z}} \\ -\varepsilon_2\omega_{\hat{x}} + \varepsilon_1\omega_{\hat{y}} + \eta\omega_{\hat{z}} \\ -\varepsilon_1\omega_{\hat{x}} - \varepsilon_2\omega_{\hat{y}} - \varepsilon_3\omega_{\hat{z}} \end{bmatrix}. \tag{A12}$$

References

[1] NIOSH, Strategic Plan for NIOSH Nanotechnology Research and Guidance: Filling the Knowledge Gaps, 2008.
[2] H.A. Whiteford, A.J. Ferrari, L. Degenhardt, V. Feigin, T. Vos, The global burden of mental, neurological and substance use disorders: an analysis from the Global Burden of Disease Study 2010, PLoS One 10 (2) (2015), e0116820.
[3] S. Peters, R.N. Carey, T.R. Driscoll, D.C. Glass, G. Benke, A. Reid, L. Fritschi, The Australian Work Exposures Study: prevalence of occupational exposure to diesel engine exhaust, Ann. Occup. Hyg. 59 (5) (2015) 600–608.
[4] D. Cavallo, A. Campopiano, G. Cardinali, S. Casciardi, P.D. Simone, D. Kovacs, B. Perniconi, G. Spagnoli, C.L. Ursini, C. Fanizza, Cytotoxic and oxidative effects induced by man-made vitreous fibers (MMVFs) in a human mesothelial cell line, Toxicology 201 (1) (2004) 219–229.
[5] N. Kobayashi, H. Izumi, Y. Morimoto, Review of toxicity studies of carbon nanotubes, J. Occup. Health 59 (5) (2017) 394–407.
[6] J. Yliniemi, R. Ramaswamy, T. Luukkonen, O. Laitinen, A. Nunes de Sousa, M. Huuhtanen, M. Illikainen, Characterization of mineral wool waste chemical composition, organic resin content and fiber dimensions: aspects for valorization, Waste Manag. 131 (2021) 323–330.
[7] C.-W. Lam, J.T. James, R. McCluskey, R.L. Hunter, Pulmonary toxicity of single-wall carbon nanotubes in mice 7 and 90 Days after intratracheal instillation, Toxicol. Sci. 77 (1) (2004) 126–134.
[8] D.B. Warheit, B.R. Laurence, K.L. Reed, D.H. Roach, G.A. Reynolds, T.R. Webb, Comparative pulmonary toxicity assessment of single-wall carbon nanotubes in rats, Toxicol. Sci. 77 (1) (2004) 117–125.
[9] A.A. Shvedova, E.R. Kisin, R. Mercer, A.R. Murray, et al., Unusual inflammatory and fibrogenic pulmonary responses to single-walled carbon nanotubes in mice, Am. J. Physiol. Lung Cell Mol. Physiol. 289 (5) (2005) L698–L708.
[10] R.R. Mercer, A.F. Hubbs, J.F. Scabilloni, L. Wang, L.A. Battelli, S. Friend, V. Castranova, D.W. Porter, Pulmonary fibrotic response to aspiration of multi-walled carbon nanotubes, Part. Fibre Toxicol. 8 (1) (2011) 21, 21.
[11] S. Smith, Y.S. Cheng, H.C. Yeh, Deposition of ultrafine particles in human tracheobronchial airways of adults and children, Aerosol Sci. Technol. 35 (2001) 697–709.
[12] J.T. Kelly, B. Asgharian, J.S. Kimbell, B.A. Wong, Particle deposition in human nasal airway replicas manufactured by different methods. Part I: inertial regime particles, Aerosol. Sci. Technol. 38 (11) (2004) 1063–1071.
[13] G.J.M. Garcia, E.W. Tewksbury, B.A. Wong, J.S. Kimbell, Interindividual variability in nasal filtration as a function of nasal cavity geometry, J. Aerosol Med. Pulm. Drug Deliv. 22 (2) (2009) 139–155.
[14] J. Rissler, E. Swietlicki, A. Bengtsson, C. Boman, J. Pagels, T. Sandström, A. Blomberg, J. Löndahl, Experimental determination of deposition of diesel exhaust particles in the human respiratory tract, J. Aerosol Sci. 48 (2012) 18–33.
[15] V. Timbrell, Deposition and retention of fibres in the human lung, Ann. Occup. Hyg. 26 (1982) 347–369.
[16] M. Lippmann, Asbestos exposure indices, Environ. Res. 46 (1) (1988) 86–106.
[17] M. Lippmann, Effects of fiber characteristics on lung deposition, retention, and disease, Environ. Health Perspect. 88 (1990) 311–317.
[18] D.W. Berman, K.S. Crump, E.J. Chatfield, J.M. Davis, A.D. Jones, The sizes, shapes, and mineralogy of asbestos structures that induce lung tumors or mesothelioma in AF/HAN rats following inhalation 1, Risk Anal. 15 (2) (1995) 181–195.
[19] Wei-Chung Su, Yung Sung Cheng, Deposition of fiber in the human nasal airway, Aerosol. Sci. Technol. 39 (9) (2005) 888–901.
[20] W.C. Su, Y.S. Cheng, Deposition of fiber in a human airway replica, J. Aerosol Sci. 37 (11) (2006) 1429–1441.
[21] Su, Wu Wei-Chung, Marijnissen Jun, C.M. Jan, Yung Sung Cheng, Deposition of man-made fibers in a human nasal airway, Aerosol. Sci. Technol. 42 (3) (2008) 173–181.
[22] H. Joshi, B.K. Jha, Modeling the spatiotemporal intracellular calcium dynamics in nerve cell with strong memory effects, Int. J. Nonlinear Sci. Numer. Stimul. (2021), https://doi.org/10.1515/ijnsns-2020-0254.
[23] Z. Zhang, C. Kleinstreuer, J.F. Donohue, C.S. Kim, Comparison of micro- and nano-size particle depositions in a human upper airway model, J. Aerosol Sci. 36 (2) (2005) 211–233.
[24] X. Xu, Y. Shang, L. Tian, W. Weng, J. Tu, Inhalation health risk assessment for the human tracheobronchial tree under pm exposure in a bus stop scene, Aerosol Air Qual. Res. 19 (6) (2019) 1365–1376.
[25] J. Dong, L. Tian, G. Ahmadi, Numerical assessment of respiratory airway exposure risks to diesel exhaust particles, Exp. Comput. Multiph. Flows 1 (1) (2019) 51–59.
[26] J. Dong, J. Li, L. Tian, J. Tu, Transport and deposition of ultrafine particles in the upper tracheobronchial tree: a comparative study between approximate and realistic respiratory tract models, Comput. Methods Biomech. Biomed. Eng. 24 (10) (2021) 1125–1135.
[27] H. Kitaoka, S. Koc, S. Tetsumoto, S. Koumo, H. Hirata, T. Kijima, 4D model generator of the human lung, in: Lung4Cer." 2013 35th Annual International Conference of the IEEE Engineering in Medicine and Biology Society (EMBC), 2013, pp. 453–456.
[28] L. Tian, G. Ahmadi, Z. Wang, P.K. Hopke, Transport and deposition of ellipsoidal fibers in low Reynolds number flows, J. Aerosol Sci. 45 (2012) 1–18.
[29] Lin Tian, Goodarz Ahmadi, Fiber transport and deposition in human upper tracheobronchial airways, J. Aerosol Sci. 60 (2013) 1–20.
[30] A. Dastan, O. Abouali, G. Ahmadi, CFD simulation of total and regional fiber deposition in human nasal cavities, J. Aerosol Sci. 69 (2014) 132–149.
[31] L. Tian, G. Ahmadi, Transport and deposition of nanofibers in human upper tracheobronchial airways, J. Aerosol Sci. 91 (2016) 22–32.
[32] L. Tian, G. Ahmadi, On nano-ellipsoid transport and deposition in the lung first bifurcation-effect of slip correction, J. Fluid Eng. 138 (10) (2016) 15–1858. FE.
[33] M.M. Tavakol, E. Ghahramani, O. Abouali, M. Yaghoubi, G. Ahmadi, Deposition fraction of ellipsoidal fibers in a model of human nasal cavity for laminar and turbulent flows, J. Aerosol Sci. 113 (2017) 52–70.
[34] L. Tian, G. Ahmadi, Computational modeling of fiber transport in human respiratory airways—a review, Exp. Comput. Multiph. Flows 3 (2021) 1–20.
[35] B. Sul, Z. Oppito, S. Jayasekera, B. Vanger, A. Zeller, M. Morris, K. Ruppert, T. Altes, V. Rakesh, S. Day, R. Robinson, J. Reifman, A. Wallqvist, Assessing airflow sensitivity to healthy and diseased lung conditions in a computational fluid dynamics model validated in vitro, J. Biomech. Eng. 140 (2018), 051009.
[36] Y.D. Shang, K. Inthavong, J.Y. Tu, Detailed micro-particle deposition patterns in the human nasal cavity influenced by the breathing zone, Comput. Fluid 114 (2015) 141–150.
[37] J. Tu, K. Inthavong, K.K.L. Wong, Geometric model reconstruction, in: Computational Hemodynamics—Theory, Modelling and Applications, Springer Netherlands, Dordrecht, 2015.
[38] J. Dong, K. Inthavong, J. Tu, Multiphase flows in biomedical applications, in: G. H. Yeoh (Ed.), Handbook of Multiphase Flow Science and Technology, Springer Singapore, Singapore, 2017.
[39] J. Tu, K. Inthavong, G. Ahmadi, The human respiratory system, in: J. Tu, K. Inthavong, G. Ahmadi (Eds.), Computational Fluid and Particle Dynamics in the Human Respiratory System, Springer Netherlands, Dordrecht, 2012.
[40] M. Spiegel, T. Redel, Y.J. Zhang, T. Struffert, J. Hornegger, R.G. Grossman, A. Doerfler, C. Karmonik, Tetrahedral vs. polyhedral mesh size evaluation on flow velocity and wall shear stress for cerebral hemodynamic simulation, Comput. Methods Biomech. Biomed. Eng. 14 (2011) 9–22.
[41] Y. Shang, J. Dong, L. Tian, K. Inthavong, J. Tu, Detailed computational analysis of flow dynamics in an extended respiratory airway model, Clin. BioMech. 61 (2019) 105–111.
[42] H. Brenner, The Stokes resistance of an arbitrary particle—IV. Arbitrary fields of flow, Chem. Eng. Sci. 19 (1964) 703–727.
[43] G.B. Jeffery, The motion of ellipsoidal particles immersed in a viscous fluid, Proc. R. Soc. A 102 (1922) 161–179.
[44] C.W. Oseen, Hydrodynamik, Akademische Verlagsgesellshaf, Leipzig, 1927.
[45] Y. Cui, J. Ravnik, M. Hriberšek, P. Steinmann, A novel model for the lift force acting on a prolate spheroidal particle in an arbitrary non-uniform flow. Part I. Lift force due to the streamwise flow shear, Int. J. Multiphas. Flow 104 (2018) 103–112.
[46] I. Gallily, A.D. Eisner, On the orderly nature of the motion of nonspherical aerosol particle I. Deposition from a laminar flow, J. Colloid Interface Sci. 68 (1979) 320–337.
[47] W. Stober, Dynamic shape factors of nonspherical aerosol particles, in: T. Mercer (Ed.), Assessment of Air Borne Particles, Charles C. Thomas Publisher, Springfield, IL, 1972, pp. 249–289.
[48] Z. Zhang, C. Kleinstreuer, Computational analysis of airflow and nanoparticle deposition in a combined nasal–oral–tracheobronchial airway model, J. Aerosol Sci. 42 (2011) 174–194.
[49] A.V. Kolanjiyil, C. Kleinstreuer, Computational analysis of aerosol-dynamics in a human whole-lung airway model, J. Aerosol Sci. 114 (2017) 301–316.

[50] H. Joshi, B.K. Jha, Advection diffusion model to study the astrocyte calcium regulation in neurodegenerative disease, Math. Eng. Sci. Aero 13 (2) (2022).
[51] H. Joshi, B.K. Jha, 2D dynamic analysis of the disturbances in the calcium neuronal model and its implications in neurodegenerative disease, Cognitive Neurodynamics (2022). https://doi.org/10.1007/s11571-022-09903-1.
[52] J. Li, J. Ma, J. Dong, W. Yang, G. Ahmadi, J. Tu, L. Tian, Microfiber transport characterization in human nasal cavity – effect of fiber length, J. Aerosol Sci. 160 (2022), 105908.
[53] J. Li, J. Ma, G. Ahmadi, J. Dong, W. Yang, J. Tu, L. Tian, Shear induced lift and rotation on MicroFiber deposition in low Reynolds number flows, J. Aerosol Sci. 167 (2022), 106094.
[54] Z. Wang, T. Guo, L. Tian, Q. Xu, S. Zhan, J. Tu, Numerical simulation on circulation flow and mass transfer inside atmospheric water drops, Appl. Therm. Eng. 118 (2008) 765–772.
[55] Z. Wang, P.K. Hopke, G. Ahmadi, Y.S. Cheng, P.A. Baron, Fibrous particle deposition in human nasal passage: the influence of particle length, flow rate, and geometry of nasal airway, J. Aerosol Sci. 39 (12) (2008) 1040–1054.
[56] H. Goldstein. Classical Mechanics, 2nd ed., Addison-Wesley, Reading: MA, 1980.
[57] P.C. Hughes. Spacecraft Attitude Dynamics, Wiley, New York, 1986.
[58] F. Fan, G. Ahmadi, A sublayer model for wall deposition of ellipsoidal particles in turbulent streams, J. Aerosol Sci. 26 (1995) 813–840.